Simulation of Arctic sea ice within the DeepMIP Eocene ensemble: Thresholds, seasonality and factors controlling sea ice development

Igor Niezgodzki [a,b,*], Gregor Knorr [b], Gerrit Lohmann [b], Daniel J. Lunt [c], Christopher J. Poulsen [d], Sebastian Steinig [c], Jiang Zhu [e], Agatha de Boer [f], Wing-Le Chan [g], Yannick Donnadieu [h], David K. Hutchinson [i], Jean-Baptiste Ladant [j], Polina Morozova [k]

[a] ING PAN - Institute of Geological Sciences Polish Academy of Sciences, Research Center in Kraków, Biogeosystem Modelling Group, Senacka 1, 31-002 Kraków, Poland
[b] Alfred Wegener Institute Helmholtz Centre for Polar and Marine Research, Bremerhaven, Germany
[c] School of Geographical Sciences, University of Bristol, Bristol, UK
[d] Department of Earth and Environmental Science, University of Michigan, 48109 Ann Arbor, USA
[e] Climate and Global Dynamics Laboratory, National Center for Atmospheric Research, Boulder, CO, USA
[f] Department of Geological Sciences, Stockholm University, Stockholm, Sweden
[g] Atmosphere and Ocean Research Institute, University of Tokyo, Tokyo, Japan
[h] Aix Marseille Univ, CNRS, IRD, INRA, Coll France, CEREGE, Aix-en-provence, France
[i] Climate Change Research Centre, University of New South Wales, Sydney, Australia
[j] Laboratoire des Sciences du Climat et de l'Environnement, LSCE/IPSL, CEA-CNRS-UVSQ, Université Paris-Saclay, Gif-sur-Yvette, France
[k] Institute of Geography, Russian Academy of Sciences, Moscow, Russia

A R T I C L E   I N F O

A B S T R A C T

The early Eocene greenhouse climate maintained by high atmospheric CO_2 concentrations serves as a testbed for future climate changes dominated by increasing CO_2 forcing. In particular, the early Eocene Arctic region is important in the context of future CO_2 driven climate warming in the northern polar region and associated shrinking Arctic sea ice. Here, we present early Eocene Arctic sea ice simulations carried out by six coupled climate models within the framework of the Deep-Time Model Intercomparison Project (DeepMIP). We find differences in sea ice responses to CO_2 changes across the ensemble and compare the results with available proxy-based sea ice reconstructions from the Arctic Ocean. Most of the models simulate seasonal sea ice presence at high CO_2 levels ($\geq$ 840 ppmv = 3× pre-industrial (PI) level of 280 ppmv). However, the threshold when sea ice permanently disappears from the ocean varies considerably between the models (from <840 ppmv to >1680 ppmv). Based on a one-dimensional energy balance model analysis we find that the greenhouse effect likely caused by increased atmospheric water vapor concentration plays an important role in the inter-model spread in Arctic winter surface temperature changes in response to a CO_2 rise from 1× to 3× the PI level. Furthermore, differences in simulated surface salinity in the Arctic Ocean play an important role in the control of local sea ice formation. These differences result from different implementations of river run-off between the models, but also from differences in the exchange of waters between a brackish Arctic and a more saline North Atlantic Ocean that are controlled by the width of the gateway between both basins. As there is no geological evidence for Arctic sea ice in the early Eocene, its presence in most of the simulations with 3× PI CO_2 level indicates either a higher CO_2 level and/or an overly weak polar sensitivity in these models.

1. Introduction

According to IPCC Shared Socio-economic Pathway (SSP) SSP5–8.5, by the end of this century atmospheric CO_2 concentration will reach 1135 ppmv (IPCC, 2021). The newest proxy-based reconstructions based on boron isotopes from planktonic foraminifera set a lower bound (95% confidence interval) on the early Eocene Climatic Optimum (EECO, ~49–53 Ma) atmospheric CO_2 at ~1170 ppmv (Anagnostou et al.,
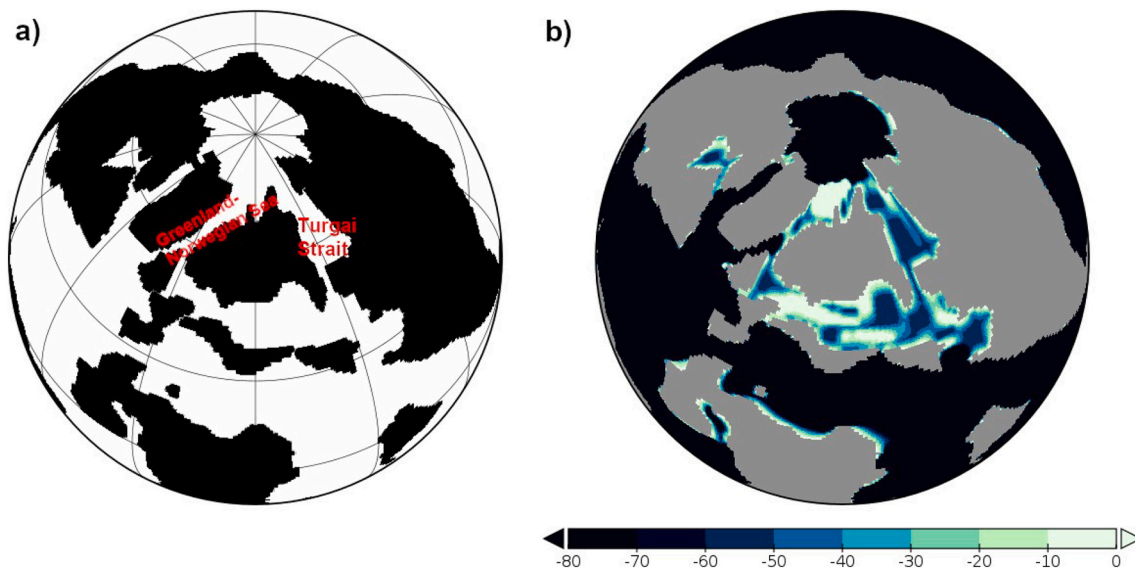
Fig. 1. a) Eocene land-sea mask of Herold et al. (2014) and b) bathymetry (m) around Arctic gateways used as an input boundary condition of each group.

2020). Therefore, early Eocene greenhouse conditions supported by the high atmospheric CO_2 concentrations are considered as one of the best analogues for future high CO_2-driven climate (Burke et al., 2018). As part of the international DeepMIP collaboration (Lunt et al., 2017, 2021), modelling groups conducted simulations of early Eocene climate with the same paleogeography and atmospheric greenhouse gas concentrations to explore inter-model variability and enable systematic investigation of early Eocene climate features.

One of the most important questions regarding near future climate is how sea ice might respond in the Arctic Ocean under elevated atmospheric CO_2 concentrations. In the last decades, Arctic sea ice has been shrinking drastically (IPCC, 2021; Simmonds and Li, 2021). The CO_2 threshold when permanent sea ice will no longer be observed in the Arctic Ocean is unknown. Based on simulations of late Miocene climate, Stein et al. (2016) indicated that at CO_2 level of 450 ppmv the Arctic Ocean was ice-free during the summer months. On the other hand, Poulsen and Zhou (2013) and Niezgodzki et al. (2019) simulated seasonal sea ice formation in the Arctic Ocean during the greenhouse of the middle and late Cretaceous. Poulsen and Zhou (2013) report seasonal ice in the Arctic Ocean at CO_2 levels up to 10× PI, while Niezgodzki et al. (2019) set the threshold for seasonal sea ice formation, independent of gateway configurations between 3× and 4× PI CO_2 levels. Therefore, it is important to investigate sea ice presence in the Arctic Ocean also during different greenhouse climates in the Earth's history with high atmospheric CO_2 levels.

Unfortunately, proxy data from the Arctic Ocean for deep-time climates are sparse. Our knowledge of the Arctic sea ice in deep-time greenhouse climates is limited and can be controversial (see Jenkyns et al. (2004) vs. Davies et al. (2009) for the Cretaceous). Additionally, some proxy-based (e.g. Tex_{86}) temperature reconstructions are controversial and can lead to overestimates of Arctic Ocean temperatures (Ho and Laepple, 2016; Jenkyns et al., 2004). Furthermore, CO_2 levels are less strictly constrained than for more recent climates. Nevertheless, recent proxy-based reconstructions suggest that seasonal sea ice was present in the Arctic Ocean as early as ~47.5 Ma while perennial (although ephemeral) sea ice was first reported for ~44 Ma (Darby, 2014; Stickley et al., 2009). However, Stein et al. (2015) dispute the presence of perennial sea ice and argue that only seasonal sea ice formed in the middle Eocene. Tripati and Darby (2018) find ice-rafted grains in the Greenland Sea originating from Greenland ~47 Ma indicating formation of glacial ice in this region. Other studies also show glacial ice around the Arctic Ocean dated from the middle Eocene (St. John, 2008;

Tripati et al., 2008). Taken together, past studies suggest that at least transient land and sea ice was present in the Arctic realm even during a high CO_2 greenhouse world. On the other hand, Eldrett et al. (2009) show that the cold month mean temperatures (CMMT) on Greenland were > 5 °C in the middle Eocene. These reconstructions preclude formation of even seasonal sea ice. Furthermore, there is no geological evidence for the presence of Arctic sea ice during the EECO. CMMT over land during early Eocene was above freezing apart from the interior of Antarctica and high altitude regions (Huber and Caballero, 2011).

DeepMIP provides a unique opportunity to investigate the early Eocene climate using a multi-model approach. Although all participating models should have been run with identical paleogeographic boundary conditions (Fig. 1), minor local adjustments (such as width/depth of the gateways or opening/closure of narrow seaways) were sometimes necessary to avoid instabilities or due to other model requirements. Even small gateway modifications can have important effects on regional climate by changing water mass exchange between the basins (e.g., Hunter et al., 2013; Knies et al., 2014; Roberts et al., 2009; Stärz et al., 2017; Vahlenkamp et al., 2018; Hutchinson et al., 2019). Furthermore, the models differ in ways that can affect the development of sea ice. One such difference is their application of river discharge models which can influence seawater salinity especially in a highly enclosed basin like the Arctic Ocean. Niezgodzki et al. (2019) show that salinity can have a decisive role in the control of sea ice formation in the Arctic Ocean by changing the freezing point temperature. Therefore, it is important to investigate the physics reasons that lead to the the differences between the sea ice modelling results across the ensemble.

Here we compare simulated Arctic sea ice across the ensemble of models participating in Eocene DeepMIP. We identify the threshold for both seasonal and perennial sea ice in the Arctic Ocean (sections 3.1 and 3.2 respectively) and discuss the physical mechanisms (section 3.3) that lead to differences in thresholds across the model ensemble. Finally, we assess our results in a geological context (section 4) by comparing them with reconstructions from proxy data.

2. Methods

The models and simulations analysed here have been previously described in the overview paper of Lunt et al. (2017, 2021). Here, we provide some details for each model that are relevant to understanding Arctic sea ice processes (see Table 1). Our study focuses on six of the eight DeepMIP models (CESM1.2_CAM5, COSMOS-landevg_r2413,

Table 1

Details of ocean components of each model included into the analyses with respective CO_2 levels sensitivity tests for each model. Additionally, threshold when sea ice disappears seasonally/permanently from the Arctic Ocean for each model is presented.

Model	Short model name	Ocean Resolution	Sea ice model parametrisation	River routing	1× CO_2	3× CO_2	4× CO_2	6× CO_2	Seasonal sea ice threshold	Permanent sea ice threshold
CESM1.2_CAM5	CESM	1.0° × 1.0°	Hunke et al. (2017)	Herold et al. (2014)	x	x		x	> 1× & < 3× CO_2	< 3× CO_2
COSMOS-landevg_r2413	COSMOS	3.0° × 1.8°	Hibler III (1979)	Hagemann and Dümenil (1998)	x	x	x		< 3× CO_2	> 4× CO_2
GFDL_CM2.1	GFDL	1.0° × 1.5°	Hunke and Dukowicz (1997), Winton (2000)	Herold et al. (2014)	x	x	x	x	< 3× CO_2	> 3× & < 4× CO_2
HadCM3b_M2.1aN	Hadley	1.25° × 1.25°	Hibler III (1979), Gordon et al. (2000)	Herold et al. (2014)	x	x			> 1× & < 2× CO_2	> 2× & < 3× CO_2
INM-CM4–8	INMCM	1.0° × 0.5°	Yakovlev (2009)	Herold et al. (2014)				x	< 6× CO_2	> 6× CO_2
IPSLCM5A2	IPSL	2.0° × 2.0°	Fichefet and Maqueda (1997), Timmermann et al. (2005)	Herold et al. (2014)	x (1.5×)	x			< 3× CO_2	> 3× CO_2
MIROC4m	MIROC	1.4° × 0.92°	Semtner Jr (1976), Hibler III (1979), Hunke and Dukowicz (1997)	Herold et al. (2014)	x	x			< 3× CO_2	> 3× CO_2

GFDL_CM2.1, HadCM3b_M2.1aN, IPSLCM5A2 and MIROC4m). We exclude NorESM1_F from the analyses because the required monthly mean model outputs were not available. Due to different resolutions of the native grids of each model, we interpolate all results to a 360 × 180 grid using nearest neighbour interpolation.

2.1. Energy flux analyses

In our analyses we apply the modified one-dimensional energy balance model used by Heinemann et al. (2009) and Lunt et al. (2012, 2021). This method allows us to separate warming due to atmospheric CO_2 changes into different components (surface albedo, non-surface albedo, heat transport convergence, long wave clouds and greenhouse effects). However, for applications of the model to seasonal timescales we must take additional constrains into account. Eq. (3) of Lunt et al. (2021) assumes that the radiation budget is closed. This is not the case for seasonal timescales due to seasonal heat storage and atmosphere-ocean heat exchange (Lee et al., 2017). Therefore, the eq. (3) of Lunt et al. (2021) will have a different form because the heat transport convergence (eq. (7) in Lunt et al. (2012)) balances net top-of-the-atmosphere short and long wave radiation imbalances only in equilibrium. As a consequence we do not differentiate between atmospheric and ocean heat flux changes.

In the following, we investigate the effect of different heat fluxes which influence DJF warming due to the CO_2 increase from 1× to 3× PI CO_2 level in each model. Instead of calculating emissivity induced warming as given in eq. (2) in Lunt et al. (2021), we split it into the greenhouse and long wave cloud effects as described by formulas (13) and (15) in Lunt et al. (2012) respectively. This allows us to separate effects of long wave clouds and water vapor contributions that are included (together with CO_2 and lapse rate) in the greenhouse effect component. It is especially important in the high latitudes where strong atmospheric moisture increase as a result of CO_2 level rise leads to surface temperature warming due to downwelling longwave radiation as shown based on the recent data for both Arctic Ocean region (Lee et al., 2017) and Antarctica (Sato and Simmonds, 2021). In our analyses we do not include any contribution of albedo effect because of the polar night in the Arctic region during DJF.

2.2. Simulation selection for inter-model comparison

Apart INMCM, all of the six above models (Table 1) provide results with 1× PI and 3× PI CO_2 levels (Table 1; except for IPSL which applies 1.5× instead of 1× PI). Therefore, we can apply the one-dimensional energy balance model analyses to these models in order to decompose

the warming due to CO_2 level change from 1× to 3× PI. We limit our analyses to simulations with 3× PI CO_2, because simulations with higher CO_2 levels were not available for all six models (Lunt et al., 2021). INMCM only provides a simulation with 6× PI CO_2 level, making energy flux analysis impossible because for one-dimensional energy balance model analyses simulations with at least two CO_2 levels are required (to investigate change in temperature). Therefore, we compare INMCM to the other results, where appropriate, but it is not included in the analysis using a one-dimensional energy balance model.

2.3. CESM virtual salt formulation

The CESM1.2 simulations used in this study include with a new representation of riverine freshwater processes from the ones documented in Zhu et al. (2019, 2020). The ocean model of CESM1.2 uses a virtual-salt formulation with the surface freshwater flux appearing in the salinity conservation equation as part of a "virtual salt flux" but not changing ocean volume. The virtual-salt formulation has a long history in ocean modelling and is known to have large errors in the salinity simulation near river mouths with large runoff (e.g., Tseng et al., 2016). As was reported in Zhu et al. (2020), CESM1.2 Eocene simulations produced negative salinity in the Arctic Ocean due to the difficulty associated with the default virtual-salt formulation. As a result, Eocene simulations in Zhu et al. (2019, 2020) used a simple artificial fix, which removes the excessive surface freshwater over the Arctic and evenly redistributes it to the global oceans. This fix removes negative salinity in the Arctic Ocean and has minor impact on global temperature and salinity distribution, but prevents us from examining regional processes in the Arctic Ocean. To remedy this, new CESM1.2 simulations were developed with an updated virtual-salt formulation (see eq. 7 from Tseng et al., 2016). In the updated formulation, local salinity was used as a reference in the part of virtual salinity flux calculation associated with river input. The updated formulation is more physical process-based, largely reduces salinity biases over places with large river runoff, and therefore has been suggested as a replacement for the default virtual-salt formulation (Tseng et al., 2016). Data from the improved CESM1.2 simulations are available in the DeepMIP data archive as version 2, which is what is used here.

3. Results

Fig. 2 depicts the sea ice net coverage area seasonal cycle for different CO_2 levels for each model. The threshold for seasonal and perennial sea ice in the Arctic Ocean varies highly across the ensemble (Table 1). In Fig. 3 we observe that there are large discrepancies between
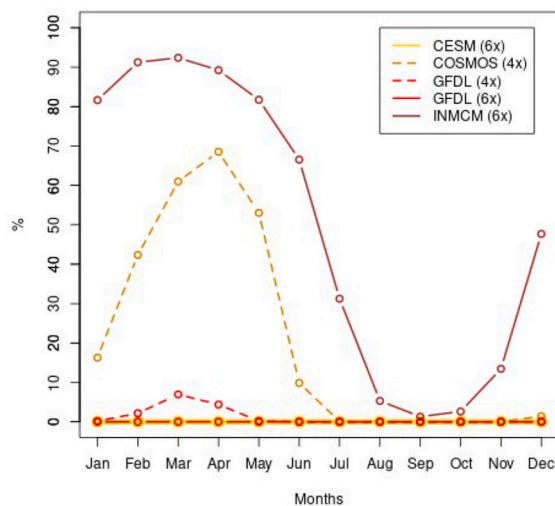
a) 1xPI Percentage of Arctic Ocean covered by sea-ice
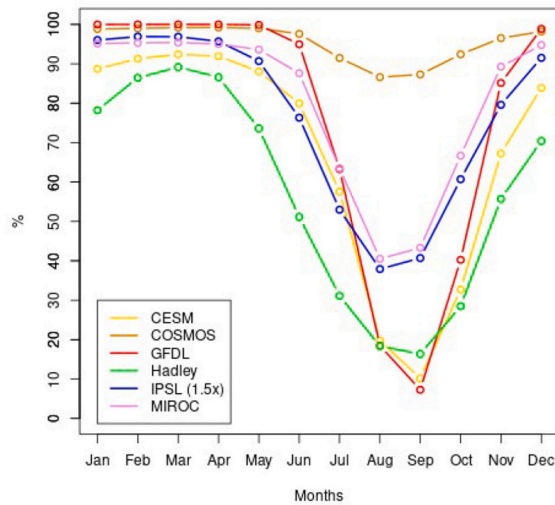
b) 3xPI Percentage of Arctic Ocean covered by sea-ice
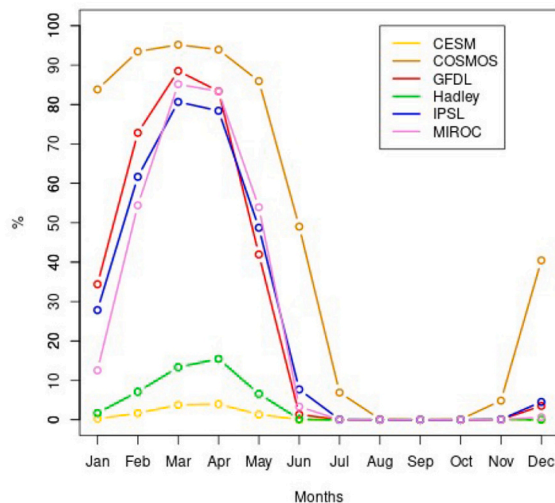
c) 4x and 6xPI Percentage of Arctic Ocean covered by sea-ice

Fig. 2. Monthly evolution of sea ice for different models for (a) $1\times$ PI, (b) $3\times$ PI and (c) 4 and $6\times$ PI CO_2 levels.

different models in the winter Arctic sea ice response to CO_2 level rise from $1\times$ to $3\times$ PI level. Below we analyse separately the seasonal (section 3.1) and permanent (section 3.2) sea ice presence in the ocean as well as the effect of freezing point temperature (section 3.3) on sea ice formation in the ocean.

3.1. Seasonal Sea ice

Fig. 2b shows that, for the Eocene simulations with $3\times$ PI CO_2 level four of six models, with CESM and Hadley as exceptions, simulate seasonal sea ice cover in the open Arctic Ocean. Maximum cover ($> 80\%$) is observed in March and April. All models are nearly ice-free ($< \sim10\%$) from July to November. In CESM and Hadley, sea ice (with maximum cover of $\sim5\%$ and $\sim 15\%$, respectively) is observed along the coastlines in March and April. Furthermore, in Hadley the $2\times$ PI CO_2 simulation is almost ice free in the Arctic Ocean from August to October (not shown).

The available simulations with higher (4 and $6\times$ PI) atmospheric CO_2 concentrations (Fig. 2c) indicate an almost ice-free Arctic Ocean in both GFDL simulations. For $4\times$ PI in COSMOS, the sea ice cover is $>40\%$ from February until May, reaching its peak ($\sim 65\%$) in April. The Arctic Ocean is almost ice-free ($< 10\%$) in COSMOS from June to December. For INMCM ($6\times$ PI CO_2), sea ice cover is $> \sim50\%$ from December to June and the Arctic Ocean is ice-free ($< 10\%$) from August to October. CESM simulation with $6\times$ PI CO_2 is fully ice free the entire year.

3.2. Perennial Sea ice

For PI CO_2 level, perennial sea ice is seen in all Eocene simulations in the open Arctic Ocean (Fig. 2a). However, in some models August and September sea ice is limited to a small area (10–20%) in the ocean. In COSMOS, the ocean is almost covered by sea ice during the entire year while in all other models, sea ice cover drops below 50% in August–September. CESM and Hadley have the least extensive sea ice cover. In the latter, maximum sea ice cover of $< \sim90\%$ is reached from February to April and the Arctic Ocean is covered in $\leq \sim50\%$ from June until November. In CESM, sea ice cover is between 80 and 90% from December until June and in particular in September the sea ice extent is limited only to the region north of North America. All other models are almost fully covered by sea ice ($> 90\%$) from December until May. The annual evolution of sea ice for $1\times$ PI CO_2 in most of the models does not fully resemble the pre-industrial control sea ice seasonal cycle. This is likely due to the different land-sea configuration in the northern polar region for these Eocene $1\times$ PI simulations and actually PI period. In the early Eocene the Arctic Ocean was more isolated from the global ocean than today. Different distribution of land masses around the Arctic Ocean support seasonal changes in the wind directions over the ocean. Seasonal wind reversals were observed around the isolated Arctic Ocean in the late Cretaceous simulations with $4\times$ PI CO_2 (Niezgodzki et al., 2019). During the late Cretaceous winter winds blow northward from the North America and Asia over the Arctic Ocean while during the summer southward from the Arctic Ocean (Fig. 8 in Niezgodzki et al., 2019) thus contributing to sea ice formation/retreat. We speculate that seasonal sea ice cycle in the early Eocene Arctic Ocean region resembles more annual sea ice evolution during other deep time period rather than present-day.

3.3. Freezing point temperature effect on sea ice

Fig. 4 shows the Temperature-Salinity (TS) diagram of DJF zonal surface temperature and salinities in the Arctic Ocean for $1\times$ and $3\times$ PI CO_2 levels in each model. For $1\times$ PI most of the profiles are covered by the freezing point temperature line. For $3\times$ PI, apart from COSMOS, all other profiles are almost entirely above the freezing point temperature. CESM's and Hadley's profile due to greater salinity and temperature (Table 2) are clearly located more above the freezing point temperature compared to other profiles. Below we analyse separately two factors
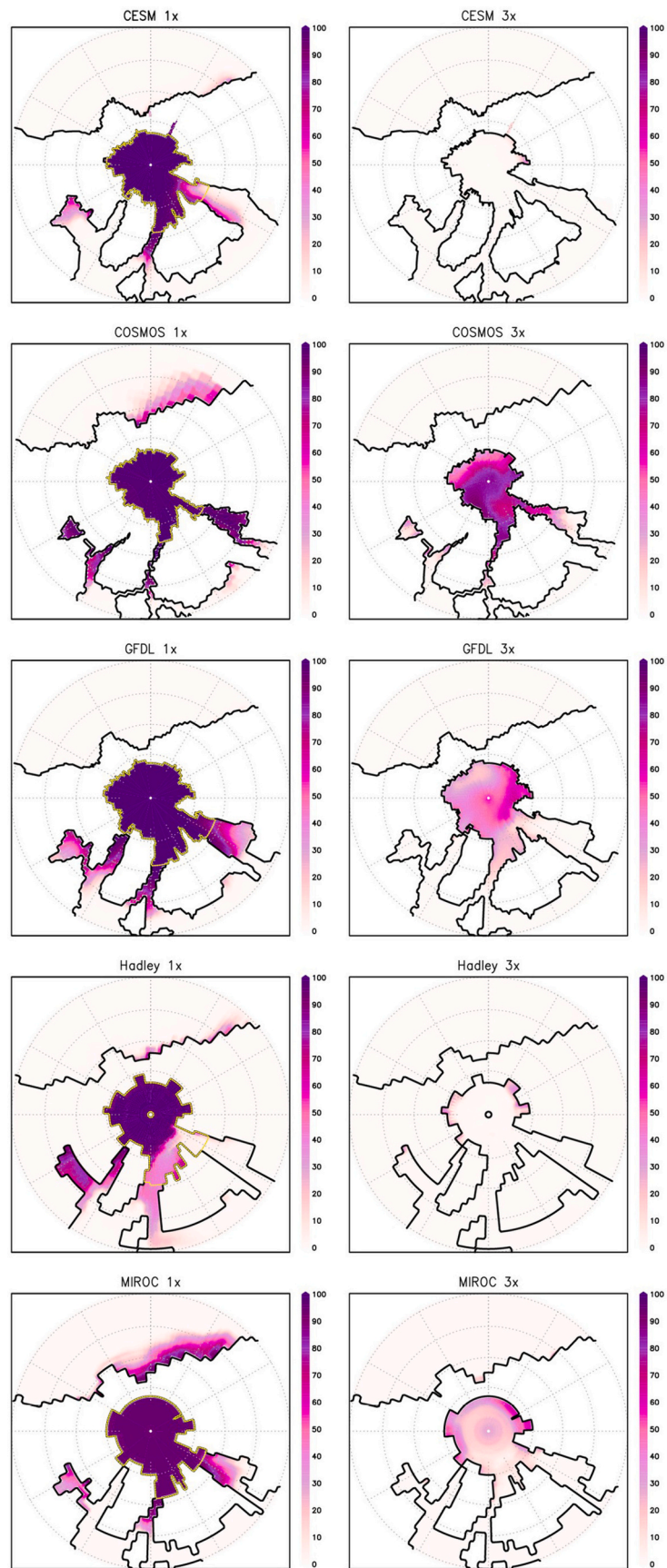
Fig. 3. DJF sea ice concentration (%) in the northern hemisphere for each model for simulations with 1× (left column) and 3× (right column) CO$_2$ levels. The yellow line in the simulations with 1× PI CO$_2$ outlines the Arctic Ocean extent. (For interpretation of the references to colour in this figure legend, the reader is referred to the web version of this article.)
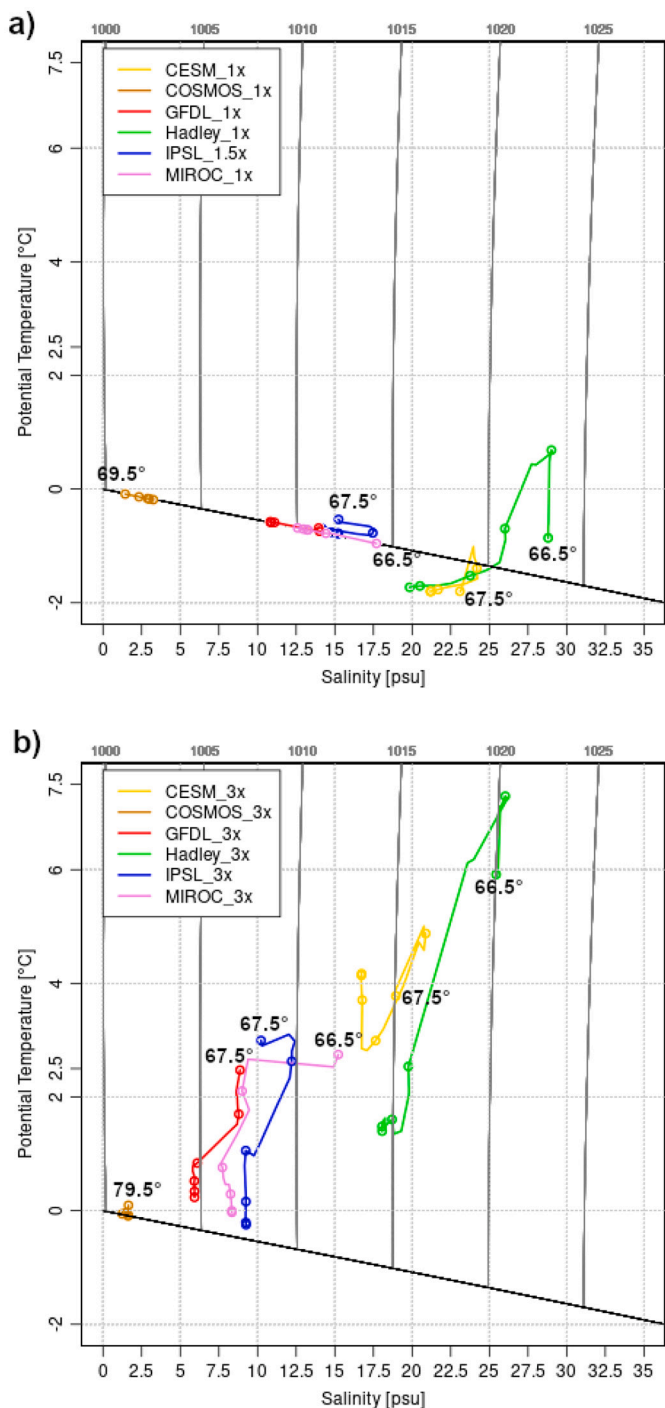
Fig. 4. TS-diagram of average DJF surface zonal mean sea surface temperatures and salinity in the Arctic Ocean for each model for a) $1\times$ and b) $3\times$ PI CO_2 levels. Degrees represent southernmost latitude of zonal mean temperature and salinity data in the Arctic Ocean. Circles on each line are set every $5°$ latitudes and on the northernmost latitude (near the North Pole).

influencing TS-profiles.

3.3.1. Salinity effect

Table 2 (col. 4) shows the width and depth of the Turgai Strait in the narrowest place as calculated on the regular grid interpolated to the $1°$ resolution using nearest neighbour interpolation in each model. CESM and Hadley have slightly deeper Turgai Strait (Table 2; Fig. 1a) than the other models. However, all the depths of the gateway are within the depth of Ekman layer which is ~60 m for the latitudes of 50–55°N (Stärz et al., 2017) where the Turgai Strait is located. The depth of the wind driven layer controls the gateways circulation regime. Therefore, differences in depth of the Turgai Strait between the models should not have a decisive impact on the salinity in the Arctic Ocean. However, in CESM and Hadley, the Turgai Strait is also wider than in other models and the inflow of waters to the strait from the North Atlantic is less inhibited by the presence of islands as compared to other models (Fig. 5). As a result, in both models we observe inflow of waters in a geostrophic regime rather than hydraulically controlled (see Jakobsson et al. (2007) for similar conditions but during the Miocene). The latter occurs when stratified fluid encounters sudden narrowing during the flow what can be observed in the enclosed water basins with estuarine type circulation (Nielsen et al., 2017). The geostrophic regime supports stronger inflow of warmer and saltier waters from North Atlantic through the Turgai Strait and into the Arctic Ocean, thus contributing to warmer and saltier surface waters as compared to other models (Fig. 5). This influx and warmer and saltier waters inhibit sea ice formation in the ocean in CESM and Hadley. Furthermore, inflow of relatively warm waters as compared to the other models through the southern Turgai Strait supports formation of local low-pressure centres over this region in Hadley. As a result, relatively strong easterlies form in the northern part of Turgai Strait which support much stronger northward currents (~1 m/s) as compared to the other models (Fig. 5). The implications of above small differences in the width of the Turgai Strait also stress the importance of precise local gateways reconstructions as an input boundary conditions for accurate regional paleoclimate simulations.

Due to model requirements, COSMOS uses a different hydrological discharge model as an input boundary condition (Hagemann and Dümenil, 1998) than provided in Lunt et al. (2017). A different hydrological discharge model might support stronger inflow of freshwater from rivers.

3.3.2. Temperature effect

As shown in Table 2, all models apart from MIROC simulate similar DJF global mean surface temperatures for $3\times$ PI CO_2 level. The SST differences between the models in the Arctic region are greater than global surface air temperature differences. To investigate the different DJF temperatures responses to CO_2 level changes over the Arctic region across the model ensemble we utilized a modified one-dimensional energy balance model (see Methods and Table 3) (Heinemann et al., 2009; Lunt et al., 2012, 2021).

We split the 2 m DJF temperature warming around the Arctic Ocean due to a CO_2 increase from $1\times$ to $3\times$ PI level into the emissivity component and the combined effect of heat transport convergence plus ocean-atmosphere heat flux. The emissivity can be further separated into the greenhouse effect (including a lapse rate effect) and long wave cloud-induced impacts. Furthermore, we estimate the combined effect of heat transport and ocean – atmosphere heat flux changes on the

Table 2

DJF global mean surface temperature, DJF sea surface temperature (SST) and salinity (SSS) in the Arctic Ocean (AO) for simulations with 3× CO_2 levels. Width of the Turgai Strait (Fig. 1a) is in the narrowest location as well as minimum sill depth in Turgai (Fig. 1b) on the grid interpolated to the resolution of 360 × 180 using nearest neighbour interpolation.

Model	DJF global mean surface temperature (°C)	DJF SST AO (°C)	DJF SSS AO (psu)	Width Turgai (km)	Minimum sill depth in Turgai (m)
CESM	24.36	3.72	17.64	869.28	45
COSMOS	24.25	−0.01	1.62	191.19	27
GFDL	25.41	0.89	6.55	342.03	35
Hadley	24.24	2.89	20.41	457.16	47.85
IPSL	24.37	0.79	9.72	136.81	35
MIROC	22.82	0.72	8.40	200.60	41.25

warming. Table 3 shows the calculated averaged DJF heat flux north of 80° N (approximate area over the Eocene Arctic Ocean) based on the one-dimensional energy balance model. The averaged DJF 2 m temperatures north of 80° N together with differences between the 3× minus 1× simulations for each model are presented for all simulations. The combined effect of heat transport and ocean-atmosphere heat fluxes (col. 8, Table 3) should be similar to the temperature differences (col. 4 in Table 3) minus total emissivity (col. 7 in Table 3). In general, these two heat fluxes should largely balance each other as ocean to atmosphere heat release during winter in the Arctic region is transported southwards by the winds to the colder surrounding continents. As a result, this combined effect plays a smaller role in the Arctic temperature rise due to CO_2 level rise compared to the emissivity-induced warming.

Table 3 (col. 4) shows that the Arctic region in CESM and Hadley experiences the strongest warming, which is > ~4 °C (CESM) and > ~6 °C (Hadley) higher than the warming in other models. This warming is mainly due to the greenhouse effect (col. 6) and associated stronger water vapor feedback under high CO_2 conditions. Furthermore, Hadley experiences also a stronger warming due to ocean to atmosphere heat flux and/or weaker cooling due to atmospheric heat transport. Nevertheless, warming in the Arctic Ocean region as a result of CO_2 level increase is mainly controlled by changes in emissivity via the greenhouse effect in all models. For IPSL, fluxes are weaker due to smaller difference in forcing associated with 1.5× and 3× PI CO_2 reference levels.

The above results have a pronounced effect on the profiles shown at the DJF TS-diagram (Fig. 4). In COSMOS, with freshwater conditions in the Arctic Ocean, the freezing point increases compared to the other profiles, while the higher salinity in CESM and Hadley decreases it. Therefore, salinity plays an important role in the control of Arctic sea ice formation. In CESM and Hadley this effect is enhanced by a stronger temperature response to CO_2 level changes as compared to the other models.

4. Discussion

Seasonal Arctic sea ice formation during the early Eocene greenhouse is unlikely (Huber and Caballero, 2011; Stein et al., 2015). However, recent data suggest that as early as the middle Eocene the Arctic Ocean was covered by ephemeral sea ice (Darby, 2014) and continental ice was present on Greenland (Tripati and Darby, 2018). The aim of DeepMIP was to simulate the early Eocene climate (~50 Ma)

(Lunt et al., 2021); nonetheless, the paleogeography changes are unlikely to have had a decisive effect on sea ice formation as compared to the middle Eocene (~47 Ma) for which sea ice was first documented. Atmospheric CO_2 concentrations in the Eocene would have been an important factor controlling sea ice formation, particularly if the levels were close to the threshold for sea ice formation. The newest proxy-based CO_2 level reconstructions for the early Eocene are lower than previously assumed and are estimated to be in the range of 1170 to 2490 ppmv (Anagnostou et al., 2020).

The CESM and Hadley show the greatest non-linearity (deviation from the logarithmic curve) in surface air temperature rise in response to CO_2 level increase (Lunt et al., 2021). Both models have no sea ice for 3× PI CO_2 and they show the greatest warming of all models (Table 3). This pronounced response is linked to feedbacks (greenhouse plus long wave clouds effects) associated with the strongest surface long wave emissivity. An additional factor for the pronounced warming in the Arctic Ocean of the two simulations with 3× PI CO_2 is linked to the relatively vigorous northward flow of warmer waters (of temperature ~ 7 °C and ~ 9.5 °C in CESM and Hadley, respectively) via a relatively wide Turgai Strait. However, it should be noted that it is difficult to separate the main driver for sea ice absence from the feedbacks, due their interdependence.

Apart from the CESM and Hadley, the threshold for total sea ice disappearance from the Arctic Ocean is >840 ppmv (Fig. 2). CESM has shown earlier high climate sensitivity and good match with temperature proxy data for the Eocene greenhouse climates (Zhu et al., 2019). Hadley is the only model among CMIP where sea ice was absent in the Arctic Ocean for the last interglacial possibly due to sophisticated sea ice melt point scheme (Guarino et al., 2020). For the IPSL and MIROC we are unable to set the upper threshold because in their maximum CO_2 level simulations (3×PI) extensive seasonal sea ice is still present (Fig. 2). However, we speculate that the threshold in these two models might be similar to the GFDL where the Arctic Ocean becomes permanently ice free for CO_2 between 3× and 4× PI levels (Fig. 2b,c). All three models simulate a similar evolution of sea ice (Fig. 2b) as well as surface salinity and temperature in the ocean (Fig. 4; Table 2) for 3× PI CO_2. A similar result for the Cretaceous can be found in Niezgodzki et al. (2019). They found the threshold for sea ice formation between 3× and 4× PI level in the simulation with closed American gateways and surface salinity in the Arctic Ocean of ~8 psu. A threshold in COSMOS when seasonal sea ice is no longer present in the Arctic Ocean during the Eocene is >1120 ppmv. This is basically identical to the minimum CO_2 level estimated for early Eocene based on the geological data (Anagnostou et al., 2020). INMCM simulates extensive sea ice during most of the year for 1680 ppmv atmospheric CO_2 concentrations which is within the range of proxy-based CO_2 level estimates. However, INMCM has relatively low climate sensitivity (Zelinka et al., 2020).

Brinkhuis et al. (2006) reconstruct episodic surface freshwater in the Arctic Ocean in the middle Eocene based on the remains of fern Azolla. Furthermore, they speculate that termination of freshwater conditions in the ocean and simultaneous warming by ~3 °C might be related to the influx of water from the adjacent oceanic basins. We speculate that the paleogeography applied in the CESM and Hadley with a stronger water exchange with North Atlantic basin due to wider and slightly deeper Arctic gateways (Table 2), might be more suitable to represent termination of the freshwater conditions in the middle Eocene as indicated by Brinkhuis et al. (2006) rather than the early Eocene. Jakobsson et al.
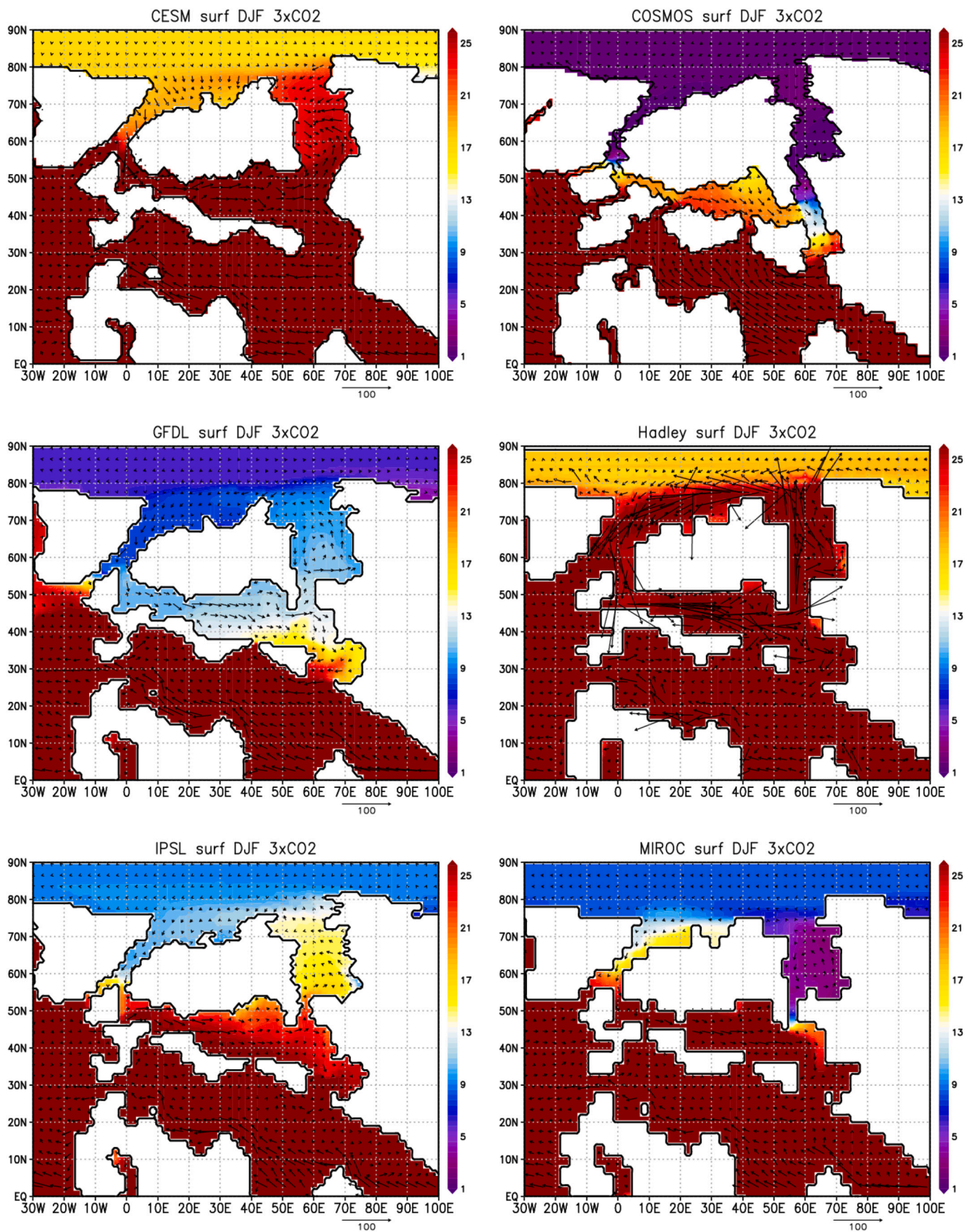
Fig. 5. Sea surface salinity (psu) and surface currents (cm/s) around the Arctic gateways for each 3× Pi simulation. Speed of the currents indicated by length of an arrow at the bottom of each figure.

Table 3

DJF 2 m temperature for 1× PI (second column) and 3× PI (third column) CO_2 levels. In the fourth column the difference between 3rd and 2nd columns. In the columns 5 to 8 are energy fluxes contributing to the warming due to CO_2 level rise from 1× to 3× PI. Note that in IPSL 1.5× PI CO_2 level was applied instead 1× PI.

Model	2 m Temp 1× PI (°C)	2 m Temp 3× PI (°C)	Difference 2 m temp 3× minus 1×	Greenhouse Effect (°C)	Clouds Long wave (°C)	Total emissivity warming (°C)	Ocean heat storage plus atmospheric heat transport (°C)
CESM	−28.07	1.75	29.82	18.66	6.82	25.48	4.34
COSMOS	−35.64	−10	25.64	12.03	6.01	18.04	7.36
GFDL	−26.88	−3.11	23.77	14.38	6.16	20.54	3.23
Hadley	−31.75	−0.18	31.57	16.09	5.79	21.88	9.69
IPSL	−22.88	−5.3	17.58	10.19	4.28	14.47	3.11
MIROC	−26.37	−3.46	22.91	14.34	5.17	19.51	3.4

(2007) show a similar circulation intensification for the Fram Strait deepening during the Miocene. Apart from the CESM and Hadley, all other models simulate either strong brackish or freshwater (COSMOS) conditions in the surface Arctic Ocean (Table 2). The low salinity in the COSMOS supports the most extensive sea ice for 1× and 3× PI CO_2 levels as well as the presence of seasonal sea ice in 4× PI CO_2. These COSMOS results are consistent with earlier simulations of Late Cretaceous climate (Niezgodzki et al., 2019) where seasonal sea ice in the Arctic Ocean was also present for 4× PI CO_2 level in the most enclosed configuration which supported freshwater conditions in the Arctic Ocean. Niezgodzki et al. (2019) also show that the small salinity increase (from ~2 psu to ~8 psu) due to gateways opening is sufficient to inhibit sea ice formation in the central Arctic Ocean due to the decrease in the freezing point temperature. Therefore, we speculate that the presence of seasonal sea ice in the Eocene COSMOS 4× PI simulation is possible due to lower salinity than in the other models.

Proxy-based salinity estimates indicate that the sea surface salinity in the Arctic Ocean was ~18–22 psu during the early Eocene (Pagani et al., 2006), in the range of CESM and Hadley simulated salinities. The strong brackish or freshwater conditions in the Arctic Ocean of other models resemble more middle Eocene freshwater Azolla phase (~50 Ma; Brinkhuis et al., 2006) rather than EECO. However, the surface temperatures of ~10 °C in the Arctic Ocean during Azolla event reconstructed based on the TEX_{86} paleothermometer (Brinkhuis et al., 2006) are significantly higher than in these simulations. Furthermore, the reconstructed CMMT for the early Eocene in the northern mid-high latitudes (north of 45° N; Huber and Caballero, 2011) are usually warmer than simulated DJF surface air temperatures (Fig. 6). All temperature estimates are ≥0 °C including 3 proxies (2 from North Greenland/Canada and 1 from Greenland-Norwegian Sea) located in the vicinity of simulated sea ice in almost each model using 3× and 4× PI CO_2 levels. These reconstructions rule out sea ice presence in the Arctic Ocean during the early Eocene. Therefore, simulated surface temperatures are too low for the EECO, possibly due to too low CO_2 levels of 3-4× PI applied in the simulations. Changes in the prescribed orbital configurations in the simulations could also reduce the data-model discrepancy. Alternatively, models can miss important processes and/or forcing (such as CH_4) or the models' sensitivity may be too low. It is also worth mentioning that the simulations where sea ice is absent (CESM and Hadley) have the greatest root mean square error (RMSE; Fig. 6). Most of the temperature reconstructions are terrestrial data that come from outside the Arctic Ocean realm and higher global scale climate sensitivity might not necessarily equate to an absence of sea ice and a better fit to high-latitude land data does not necessarily line up with agreement on sea ice proxies.

In summary, apart from the CESM and Hadley, all models simulate

seasonal Arctic sea ice cover when CO_2 levels are at (INMCM) or close to (COSMOS, GFDL, IPSL, MIROC) the range of proxy-based CO_2 estimates for early Eocene. However, there was no sea ice presence in the Arctic Ocean during this time as indicated by geological data (Huber and Caballero, 2011; Stein et al., 2015). This mismatch could indicate that either atmospheric CO_2 concentrations were higher during the early Eocene than applied in these simulations or the models' sensitivities are too low. A decrease in atmospheric CO_2 concentration toward the end of the Eocene (Beerling and Royer, 2011), with simultaneous cooling of sea surface temperatures (Stein et al., 2015) likely triggered seasonal sea ice formation in the Arctic Ocean in the middle Eocene. Narrow and shallow gateways (as in four of six models) between the Arctic and North Atlantic Oceans support limited water exchange between these two basins. As a result, the Arctic Ocean was fresher in these models which could enhance seasonal Arctic sea ice presence during the middle Eocene. We speculate that the CESM and Hadley simulations are more suitable to represent EECO due to the wider Turgai Strait. It enables more vigorous water exchange between the Arctic and North Atlantic Oceans, thus supporting, in agreement with reconstructions, higher salinity in the Arctic Ocean than in four other models with narrow Turgai Strait. The COSMOS, GFDL, IPSL and MIROC could represent middle Eocene conditions with seasonal sea ice presence in the Arctic Ocean. CO_2 levels in these simulations (of 3-4× PI) might be within the range of the middle Eocene atmospheric CO_2 concentrations (that declined since the end of EECO; Anagnostou et al., 2020). Alternatively, these models could be used to simulate the middle Eocene freshwater Azolla event (although higher CO_2 levels should be applied). CESM and Hadley could represent termination of the Azolla phase.

5. Conclusions

We compare simulated sea ice presence in the Arctic Ocean during the greenhouse of the early Eocene using a suite of simulations conducted within DeepMIP (Lunt et al., 2021). Although the simulations provide diverging CO_2 thresholds for seasonal sea ice (from <840 ppmv to >1680 ppmv), most of the models simulate sea ice in the central Arctic Ocean for the higher (≥ 840 ppmv) CO_2 levels of the Eocene. The differences in the thresholds result from the different responses of polar winter temperatures to CO_2 increase and salinity differences in the Arctic Ocean across the ensemble. The salinity differences are dominated by width of the gateways between the Arctic and North Atlantic Oceans. Since there are no geological data that support sea ice in the Arctic Ocean before the middle Eocene, the atmospheric CO_2 level during the early Eocene was likely higher than 3× PI CO_2 applied in our simulations or four models in our DeepMIP ensemble (apart from CESM and Hadley) indicate too weak polar sensitivity. The simulations with
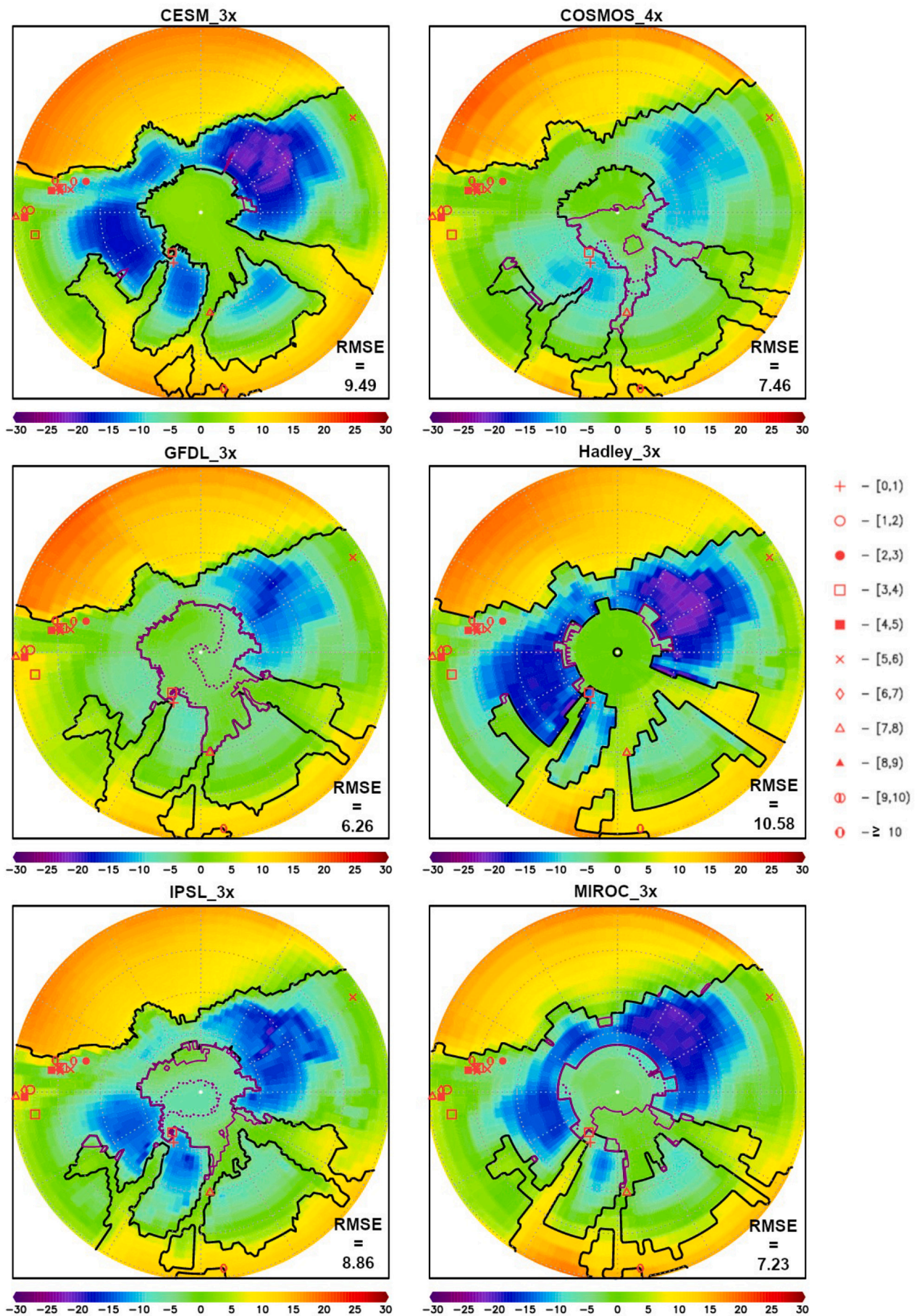
Fig. 6. Simulated DJF surface air temperatures in °C vs. proxy based (red marks) cold month mean temperatures from Huber and Caballero (2011) to the north of 45° N. The temperature ranges (°C) for each mark are shown in the right. Root mean square error (°C) for each simulation shown in the lower right corner of each plot. Solid and dotted violet lines indicate the sea ice line where concentration is >15 and > 50% respectively. (For interpretation of the references to colour in this figure legend, the reader is referred to the web version of this article.)

sea ice presence might be more suitable to represent middle Eocene climatic conditions because declining CO_2 level which started at the end of the EECO could fall in the range of CO_2 levels applied in our simulations. Furthermore, a narrow Turgai Strait in the four models limits the water exchange between the Arctic and North Atlantic Oceans and supports near-freshwater conditions in the Arctic Ocean as reported during middle Eocene Azolla event. We conclude that the exchange between the relatively fresh Arctic Ocean and the more saline North Atlantic Ocean is controlled by the width of the gateway and is thus very sensitive to the model configuration and setup. As a logical next step, we will perform a multi-scale approach (Lohmann et al., 2020) in order to examine the effect of narrow gateways in the framework of global Eocene paleoclimate modelling.

Declaration of Competing Interest

The authors declare that they have no known competing financial interests or personal relationships that could have appeared to influence the work reported in this paper.

References

Anagnostou, E., John, E.H., Babila, T.L., Sexton, P.F., Ridgwell, A., Lunt, D.J., Pearson, P. N., Chalk, T.B., Pancost, R.D., Foster, G.L., 2020. Proxy evidence for state-dependence of climate sensitivity in the Eocene greenhouse. Nat. Commun. 11 (1) https://doi.org/10.1038/s41467-020-17887-x.

Beerling, D.J., Royer, D.L., 2011. Convergent cenozoic CO 2 history. Nat. Geosci. 4 (7), 418–420. https://doi.org/10.1038/ngeo1186.

Brinkhuis, H., Schouten, S., Collinson, M.E., Sluijs, A., Damsté, J.S.S., Dickens, G.R., Huber, M., Cronin, T.M., Onodera, J., Takahashi, K., Bujak, J.P., Stein, R., Van Der Burgh, J., Eldrett, J.S., Harding, I.C., Lotter, A.F., Sangiorgi, F., Van Cittert, H.V.K., De Leeuw, J.W., et al., 2006. Episodic fresh surface waters in the Eocene Arctic Ocean. Nature 441 (7093), 606–609. https://doi.org/10.1038/nature04692.

Burke, K.D., Williams, J.W., Chandler, M.A., Haywood, A.M., Lunt, D.J., Otto-Bliesner, B. L., 2018. Pliocene and Eocene provide best analogs for near-future climates. Proc. Natl. Acad. Sci. 115 (52), 13288–13293. https://doi.org/10.1073/pnas.1809600115.

Darby, D.A., 2014. Ephemeral formation of perennial sea ice in the Arctic Ocean during the middle Eocene. Nat. Geosci. 7 (3), 210–213. https://doi.org/10.1038/ngeo2068.

Davies, A., Kemp, A.E.S., Pike, J., 2009. Late cretaceous seasonal ocean variability from the Arctic. Nature 460 (7252), 254–258. https://doi.org/10.1038/nature08141.

Eldrett, J.S., Greenwood, D.R., Harding, I.C., Huber, M., 2009. Increased seasonality through the Eocene to Oligocene transition in northern high latitudes. Nature 459 (7249), 969–973. https://doi.org/10.1038/nature08069.

Fichefet, T., Maqueda, M.M., 1997. Sensitivity of a global sea ice model to the treatment of ice thermodynamics and dynamics. J. Geophys. Res. Oceans 102 (C6), 12609–12646. https://doi.org/10.1029/97JC00480.

Gordon, C., Cooper, C., Senior, C.A., Banks, H., Gregory, J.M., Johns, T.C., Wood, R.A., 2000. The simulation of SST, sea ice extents and ocean heat transports in a version of the Hadley Centre coupled model without flux adjustments. Clim. Dyn. 16 (2), 147–168. https://doi.org/10.1007/s003820050010.

Guarino, M.V., Sime, L.C., Schröeder, D., Malmierca-Vallet, I., Rosenblum, E., Ringer, M., Sellar, A., 2020. Sea-ice-free Arctic during the last Interglacial supports fast future loss. Nat. Clim. Chang. 10 (10), 928–932. https://doi.org/10.1038/s41558-020-0865-2.

Hagemann, S., Dümenil, L., 1998. A parametrization of the lateral waterflow for the global scale. Clim. Dyn. 14 (1), 17–31. https://doi.org/10.1007/s003820050205.

Heinemann, M., Jungclaus, J.H., Marotzke, J., 2009. Warm Paleocene/Eocene climate as simulated in ECHAM5/MPI-OM. Clim. Past 5 (4), 785–802. https://doi.org/10.5194/cp-5-785-2009.

Herold, N., Buzan, J., Seton, M., Goldner, A., Green, J.A.M., Müller, R.D., Huber, M., 2014. A suite of early Eocene (~ 55 Ma) climate model boundary conditions. Geosci. Model Dev. 7 (5), 2077–2090. https://doi.org/10.5194/gmd-7-2077-2014.

Hibler III, W.D., 1979. A dynamic thermodynamic sea ice model. J. Phys. Oceanogr. 9 (4), 815–846. https://doi.org/10.1175/1520-0485(1979)009<0815:ADTSIM>2.0. CO;2.

Ho, S.L., Laepple, T., 2016. Flat meridional temperature gradient in the early Eocene in the subsurface rather than surface ocean. Nat. Geosci. 9 (8), 606–610. https://doi.org/10.1038/ngeo2763.

Huber, M., Caballero, R., 2011. The early Eocene equable climate problem revisited. Clim. Past 7 (2), 603–633. https://doi.org/10.5194/cp-7-603-2011.

Hunke, E.C., Dukowicz, J.K., 1997. An elastic–viscous–plastic model for sea ice dynamics. J. Phys. Oceanogr. 27 (9), 1849–1867. https://doi.org/10.1175/1520-0485(1997)027<1849:AEVPMF>2.0.CO;2.

Hunke, E., Lipscomb, W., Jones, P., Turner, A., Jeffery, N., Elliott, S., 2017. CICE, the Los Alamos Sea ice model (no. CICE; 005315WKSTN00). Los Alamos National Lab. (LANL), Los Alamos, NM (United States).

Hunter, S.J., Haywood, A.M., Valdes, P.J., Francis, J.E., Pound, M.J., 2013. Modelling equable climates of the late cretaceous: can new boundary conditions resolve data-model discrepancies? Palaeogeogr. Palaeoclimatol. Palaeoecol. 392, 41–51. https://doi.org/10.1016/j.palaeo.2013.08.009.

Hutchinson, D.K., Coxall, H.K., O'Regan, M., Nilsson, J., Caballero, R., de Boer, A.M., 2019. Arctic closure as a trigger for Atlantic overturning at the Eocene-Oligocene transition. Nat. Commun. 10 (1), 1–9. https://doi.org/10.1038/s41467-019-11828-z.

IPCC, 2021. In: Masson-Delmotte, V., Zhai, P., Pirani, A., Connors, S.L., Péan, C., Berger, S., Caud, N., Chen, Y., Goldfarb, L., Gomis, M.I., Huang, M., Leitzell, K., Lonnoy, E., Matthews, J.B.R., Maycock, T.K., Waterfield, T., Yelekçi, O., Yu, R., Zhou, B. (Eds.), Climate Change 2021: the Physical Science Basis. Contribution of Working Group I to the Sixth Assessment Report of the Intergovernmental Panel on climate Change. Cambridge University Press (In Press).

Jakobsson, M., Backman, J., Rudels, B., Nycander, J., Frank, M., Mayer, L., Moran, K., 2007. The early Miocene onset of a ventilated circulation regime in the Arctic Ocean. Nature 447 (7147), 986–990. https://doi.org/10.1038/nature05924.

Jenkyns, H.C., Forster, A., Schouten, S., Sinninghe Damsté, J.S., 2004. High temperatures in the late cretaceous Arctic Ocean. Nature 432 (7019), 888–892. https://doi.org/10.1038/nature03143.

Knies, J., Mattingsdal, R., Fabian, K., Grøsfjeld, K., Baranwal, S., Husum, K., De Schepper, S., Vogt, C., Andersen, N., Matthiessen, J., Andreassen, K., Jokat, W., Nam, S. Il, Gaina, C., 2014. Effect of early Pliocene uplift on late Pliocene cooling in the Arctic-Atlantic gateway. Earth Planet. Sci. Lett. 387, 132–144. https://doi.org/10.1016/j.epsl.2013.11.007.

Lee, S., Gong, T., Feldstein, S.B., Screen, J.A., Simmonds, I., 2017. Revisiting the cause of the 1989–2009 Arctic surface warming using the surface energy budget: Downward infrared radiation dominates the surface fluxes. Geophys. Res. Lett. 44 (20), 10–654. https://doi.org/10.1002/2017GL075375.

Lohmann, G., Butzin, M., Eissner, N., Shi, X., Stepanek, C., 2020. Abrupt climate and weather changes across time scales. Paleoceanogr. Paleoclimatol. 35 (9) https://doi.org/10.1029/2019PA003782 e2019PA003782.

Lunt, D.J., Jones, T.D., Heinemann, M., Huber, M., LeGrande, A., Winguth, A., Loptson, C., Marotzke, J., Roberts, C.D., Tindall, J., Valdes, P., Winguth, C., 2012. A model-data comparison for a multi-model ensemble of early Eocene atmosphere-ocean simulations: EoMIP. Clim. Past 8 (5), 1717–1736. https://doi.org/10.5194/cp-8-1717-2012.

Lunt, Daniel J., Huber, M., Anagnostou, E., Baatsen, M.L.J., Caballero, R., DeConto, R., Dijkstra, H.A., Donnadieu, Y., Evans, D., Feng, R., Foster, G.L., Gasson, E., Von Der Heydt, A.S., Hollis, C.J., Inglis, G.N., Jones, S.M., Kiehl, J., Turner, S.K., Korty, R.L., et al., 2017. The DeepMIP contribution to PMIP4: Experimental design for model simulations of the EECO, PETM, and pre-PETM (version 1.0). Geosci. Model Dev. 10 (2), 889–901. https://doi.org/10.5194/gmd-10-889-2017.

Lunt, Daniel J., Bragg, F., Le Chan, W., Hutchinson, D.K., Ladant, J.B., Morozova, P., Niezgodzki, I., Steinig, S., Zhang, Z., Zhu, J., Abe-Ouchi, A., Anagnostou, E., De Boer, A.M., Coxall, H.K., Donnadieu, Y., Foster, G., Inglis, G.N., Knorr, G., Langebroek, P.M., Lear, C.H., Lohman, G., Poulsen, C.J., Otto-Bliesner, B.L., 2021. DeepMIP: Model intercomparison of early Eocene climatic optimum (EECO) large-scale climate features and comparison with proxy data. Clím. Past 17 (1), 203–227. https://doi.org/10.5194/cp-17-203-2021.

Nielsen, M.H., Vang, T., Lund-Hansen, L.C., 2017. Internal hydraulic control in the Little Belt, Denmark–observations of flow configurations and water mass formation. Ocean Sci. 13 (6), 1061–1075. https://doi.org/10.5194/os-13-1061-2017.

Niezgodzki, I., Tyszka, J., Knorr, G., Lohmann, G., 2019. Was the Arctic Ocean ice free during the latest cretaceous? The role of CO2 and gateway configurations. Glob. Planet. Chang. 177 (December 2018), 201–212. https://doi.org/10.1016/j.gloplacha.2019.03.011.

Pagani, M., Pedentchouk, N., Huber, M., Sluijs, A., Schouten, S., Brinkhuis, H., Dickens, G.R., 2006. Arctic hydrology during global warming at the Palaeocene/Eocene thermal maximum. Nature 442 (7103), 671–675. https://doi.org/10.1038/nature05043.

Poulsen, C.J., Zhou, J., 2013. Sensitivity of Arctic climate variability to mean state: insights from the cretaceous. J. Clim. 26 (18), 7003–7022. https://doi.org/10.1175/JCLI-D-12-00825.1.

Roberts, C.D., LeGrande, A.N., Tripati, A.K., 2009. Climate sensitivity to Arctic seaway restriction during the early Paleogene. Earth Planet. Sci. Lett. 286 (3–4), 576–585. https://doi.org/10.1016/j.epsl.2009.07.026.

Sato, K., Simmonds, I., 2021. Antarctic skin temperature warming related to enhanced downward longwave radiation associated with increased atmospheric advection of moisture and temperature. Environ. Res. Lett. 16 (6), 064059 https://doi.org/10.1088/1748-9326/ac0211.

Semtner Jr., A.J., 1976. A model for the thermodynamic growth of sea ice in numerical investigations of climate. J. Phys. Oceanogr. 6 (3), 379–389. https://doi.org/10.1175/15200485(1976)006<0379:AMFTTG>2.0.CO;2.

Simmonds, I., Li, M., 2021. Trends and variability in polar sea ice, global atmospheric circulations, and baroclinicity. Ann. N. Y. Acad. Sci. 1504 (1), 167–186. https://doi.org/10.1111/nyas.14673.

St. John, K., 2008. Cenozoic ice-rafting history of the Central Arctic Ocean: Terrigenous sands on the Lomonosov Ridge. Paleoceanography 23 (1), 1–12. https://doi.org/10.1029/2007PA001483.

Stärz, M., Jokat, W., Knorr, G., Lohmann, G., 2017. Threshold in North Atlantic-Arctic Ocean circulation controlled by the subsidence of the Greenland-Scotland Ridge. Nat. Commun. 8, 1–13. https://doi.org/10.1038/ncomms15681.

Stein, R., Jokat, W., Niessen, F., Weigelt, E., 2015. Exploring the long-term Cenozoic Arctic Ocean climate history: a challenge within the International Ocean Discovery Program (IODP). Arktos 1 (1), 3. https://doi.org/10.1007/s41063-015-0012-x.

Stein, R., Fahl, K., Schreck, M., Knorr, G., Niessen, F., Forwick, M., Gebhardt, C., Jensen, L., Kaminski, M., Kopf, A., Matthiessen, J., Jokat, W., Lohmann, G., 2016. Evidence for ice-free summers in the late Miocene Central Arctic Ocean. Nat. Commun. 7, 1–13. https://doi.org/10.1038/ncomms11148.

Stickley, C.E., St John, K., Koç, N., Jordan, R.W., Passchier, S., Pearce, R.B., Kearns, L.E., 2009. Evidence for middle Eocene Arctic Sea ice from diatoms and ice-rafted debris. Nature 460 (7253), 376–379. https://doi.org/10.1038/nature08163.

Timmermann, R., Goosse, H., Madec, G., Fichefet, T., Ethe, C., Duliere, V., 2005. On the representation of high latitude processes in the ORCA-LIM global coupled sea ice–ocean model. Ocean Model 8 (1–2), 175–201. https://doi.org/10.1016/j.ocemod.2003.12.009.

Tripati, A., Darby, D., 2018. Evidence for ephemeral middle Eocene to early Oligocene Greenland glacial ice and pan-Arctic Sea ice. Nat. Commun. 9 (1), 1–11. https://doi.org/10.1038/s41467-018-03180-5.

Tripati, A.K., Eagle, R.A., Morton, A., Dowdeswell, J.A., Atkinson, K.L., Bahé, Y., Dawber, C.F., Khadun, E., Shaw, R.M.H., Shorttle, O., Thanabalasundaram, L., 2008. Evidence for glaciation in the Northern Hemisphere back to 44 Ma from ice-rafted debris in the Greenland Sea. Earth Planet. Sci. Lett. 265 (1–2), 112–122. https://doi.org/10.1016/j.epsl.2007.09.045.

Tseng, Y.H., Bryan, F.O., Whitney, M.M., 2016. Impacts of the representation of riverine freshwater input in the community earth system model. Ocean Model 105, 71–86. https://doi.org/10.1016/j.ocemod.2016.08.002.

Vahlenkamp, M., Niezgodzki, I., De Vleeschouwer, D., Lohmann, G., Bickert, T., Pälike, H., 2018. Ocean and climate response to North Atlantic seaway changes at the onset of long-term Eocene cooling. Earth Planet. Sci. Lett. 498, 185–195. https://doi.org/10.1016/j.epsl.2018.06.031.

Winton, M., 2000. A reformulated three-layer sea ice model. J. Atmos. Ocean. Technol. 17 (4), 525–531. https://doi.org/10.1175/1520-0426(2000)017<0525:ARTLSI>2.0.CO;2.

Yakovlev, N.G., 2009. Reproduction of the large-scale state of water and sea ice in the Arctic Ocean in 1948–2002: part I. Numerical model. *Izvestiya*. Atmos. Oceanic Phys. 45 (3), 357–371. https://doi.org/10.1134/S0001433809030098.

Zelinka, M.D., Myers, T.A., McCoy, D.T., Po-Chedley, S., Caldwell, P.M., Ceppi, P., Taylor, K.E., 2020. Causes of higher climate sensitivity in CMIP6 models. Geophys. Res. Lett. 47 (1) https://doi.org/10.1029/2019GL085782 e2019GL085782.

Zhu, J., Poulsen, C.J., Tierney, J.E., 2019. Simulation of Eocene extreme warmth and high climate sensitivity through cloud feedbacks. Sci. Adv. 5 (9), eaax1874. https://doi.org/10.1016/j.epsl.2020.116164.

Zhu, J., Poulsen, C.J., Otto-Bliesner, B.L., Liu, Z., Brady, E.C., Noone, D.C., 2020. Simulation of early Eocene water isotopes using an Earth system model and its implication for past climate reconstruction. Earth Planet. Sci. Lett. 537, 116164 https://doi.org/10.1016/j.epsl.2020.116164.